Final draft submitted to:

CIRP Annals
Manufacturing Technology

Design of a 4-DOF hybrid PKM module for large structural component assembly

T. Huang (2) [a,b,*], P.F. Wang [a], X.M. Zhao [a], D.G. Chetwynd [b]

[a]School of Mechanical Engineering, Tianjin University, Tianjin 300072, China
[b]School of Engineering, The University of Warwick, Coventry CV4 7AL, UK

ABSTRACT
This paper presents a novel 4-DOF hybrid parallel kinematic machine (PKM), named Bicept, comprising a 2-DOF parallel mechanism plus a 2-DOF rotating head. The PKM is designed as a rigid yet compact module that can act as a robot cell moving along a long track for aircraft structural component assembly, a wing box for example. Dimensional synthesis of the 2-DOF parallel mechanism is carried out to achieve a relatively good kinematic performance within a prescribed task workspace that has a large width/height ratio. Then, using commercial CAE software, rigid body dynamics and stiffness analyses are carried out for motor sizing and performance evaluation of a full-size virtual prototype.

KEYWORDS
Parallel kinematic machines, virtual prototype design, assembly

1. Introduction

Drilling and riveting in the assembly process of large structural components, a wing box for example, is a challenging problem in aircraft manufacturing [1,3]. Such work is mostly done manually, which inevitably affects the safety, quality, productivity and reliability. One way to solve the problem is to use a dedicated automatic riveting machine with "C" layout, usually equipped with a gantry-like multiple-axis worktable. With the increase in the component sizes, use of such a layout becomes impractical. An alternative is to use robot work cells along very long reference tracks that form the base of an assembly system [4,5]. This idea has been demonstrated by very successful applications of one or two face-to-face placed Tricept robots [6-8] in wing assembly. Although extensive research and application activities have been carried out on the Tricept robot, it is quite surprising that little attention has been paid to its simplified 2D version that may be more cost effective in many practical applications since one axis can be saved in comparison with the Tricept solution.

Motivated by this idea, this paper presents a 4-DOF PKM module named the Bicept [9,10] (see Fig.1) that can be used to configure a robot cell for aircraft wing box assembly (see Fig.2). The dimensional synthesis of the 2-DOF parallel mechanism is investigated using virtual machine tool technology [11]. Then, rigid body dynamics and stiffness analyses are carried out for performance evaluation of a full-size virtual prototype, using commercial CAE software.

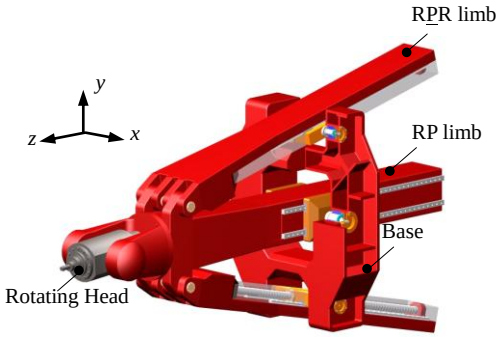

Fig.1 3D model of the Bicept robot

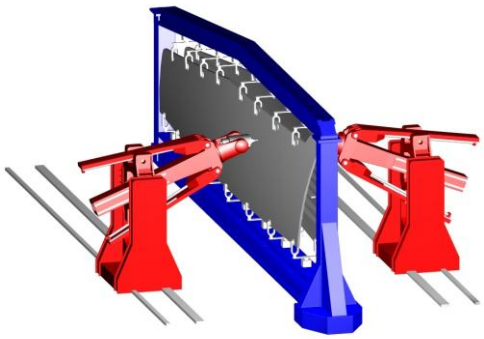

Fig.2 The Conceptual design of an aircraft wing box assembly system using two Bicept robots

2. Conceptual design

Fig.1 shows a CAD model of the proposed 4-DOF Bicept

* Corresponding author

robot which consists of a 2-DOF planar parallel mechanism to position the moving platform, and a 2-DOF rotating head attached to the moving platform to achieve orientation capability about two orthogonal axes. The 2-DOF parallel mechanism is composed of a moving platform, two active RPR limbs and a passive RP limb that is rigidly connected with the platform. Here, R and P denote revolute and prismatic joints, and the underlined P denotes an actuated prismatic joint. Manipulated by means of two servomotors situated on the RPR limbs, the reference point at the center of the rotating head undergoes translation along the axis of the P joint and rotation about the axis of R joint of the RP limb. Thus, incorporating a 2D rotating head with A/C axis arrangement can provide 4-DOF movement capabilities. An end-effector such as a spindle, electro-magnetic riveting gun, etc. can be mounted on the rotating head to implement various manufacturing operations.

In order to achieve a compact, light-weight yet rigid design, the revolute joints connecting the limbs with the base are of quite complex, high-specification design. There is a bearing to each side, with its inner ring rigidly registered to the carriage of the RPR limb via a half shaft. The carriage also serves as the nut of the lead-screw assembly and as one element of a ball guideway against the limb body. The cross section of the RPR limb is designed as a narrow rectangle in order to achieve sufficient bending and torsional rigidities against out-of-plane motion. The RP limb is made stronger than the RPR limb by using a hollow right rectangle to sustain the bending and torsional moments within and out of the motion plane. Similar to the application of the Tricept robot in the aerospace industry, the Bicept robot can be mounted on a column to configure a robot cell as shown in Fig.2. Two robot cells placed face-to-face can then form a wing box assembling system by adding translational motions along the long reference tracks.

3. Kinematic design

In this section, the kinematic design of the 2-DOF parallel mechanism within the Bicept robot is carried out to determine dimensional parameters such that good global kinematic performance can be achieved in a relatively large prescribed workspace, specifically having a large width/height ratio.

3.1 Inverse kinematics

In order to evaluate the kinematic performance of the 2-DOF parallel mechanism, it is necessary to formulate kinematic equations for the inverse position and velocity analyses.

In the $O-yz$ coordinate system shown in Fig.3, the position vector $\boldsymbol{r}$ of point P can be expressed by

$$\boldsymbol{r} = \rho + e\ \boldsymbol{u} \tag{1}$$

$$\boldsymbol{r} = -a\,\mathrm{sgn}(i)\boldsymbol{Q}\boldsymbol{u} + e\boldsymbol{u} + q_i\boldsymbol{u}_i + b\,\mathrm{sgn}(i)\boldsymbol{e}_2, \quad i = 1,\ 2 \tag{2}$$

where q_i, ρ, $\boldsymbol{u}_i$ and $\boldsymbol{u}$ are the length and unit vector of the ith RPR and the RP limbs, respectively; $a = \overline{O'A_i}$, $b = \overline{OB_i}$ and $e = \overline{O'P}$;

$$\boldsymbol{u}_i = \begin{bmatrix}\cos\theta_i & \sin\theta_i\end{bmatrix}^{\mathrm{T}}, \quad \boldsymbol{u} = \begin{bmatrix}\cos\theta & \sin\theta\end{bmatrix}^{\mathrm{T}}$$

$$\mathrm{sgn}(i) = \begin{cases}1 & i=1\\ -1 & i=2\end{cases}, \quad \boldsymbol{e}_2 = \begin{bmatrix}0 & 1\end{bmatrix}^{\mathrm{T}}, \quad \boldsymbol{Q} = \begin{bmatrix}0 & -1\\ 1 & 0\end{bmatrix}$$

Given $\boldsymbol{r}$, we have

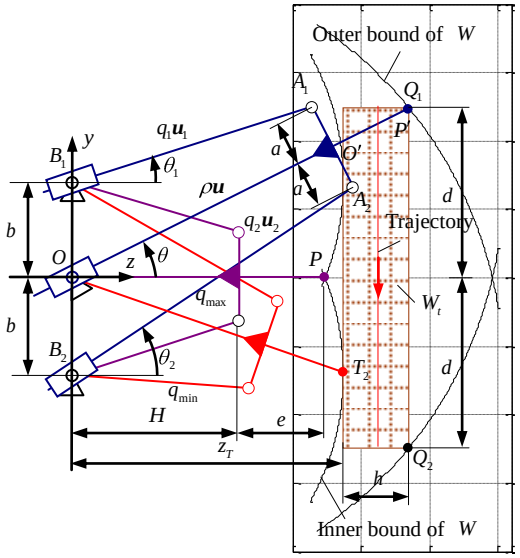

Fig. 3. Schematic diagram and workspace of the 2-DOF parallel mechanism within the Bicept robot

$$\boldsymbol{u} = \frac{1}{\rho + e}\boldsymbol{r}\ ,\ \rho = |\boldsymbol{r}| - e\ ,\quad \theta = \arctan(u_y / u_z) \tag{3}$$

and then

$$q_i = \left|\rho\boldsymbol{u} + a\,\mathrm{sgn}(i)\boldsymbol{Q}\boldsymbol{u} - b\,\mathrm{sgn}(i)\boldsymbol{e}_2\right| \tag{4}$$

$$\boldsymbol{u}_i = \left(\rho\boldsymbol{u} + a\,\mathrm{sgn}(i)\boldsymbol{Q}\boldsymbol{u} - b\,\mathrm{sgn}(i)\boldsymbol{e}_2\right) / q_i\ ,\ \theta_i = \arctan(u_{iy} / u_{iz})$$

Differentiating (1) and (2) with respect to time and taking dot products with the velocity unit vectors yields, after some manipulation, the velocity model of the parallel mechanism

$$\dot{\boldsymbol{q}} = \boldsymbol{J}\dot{\boldsymbol{r}} \tag{5}$$

$$\boldsymbol{J} = \begin{bmatrix}\boldsymbol{u}_1^{\mathrm{T}} - \dfrac{1}{\rho+e}\boldsymbol{u}_1^{\mathrm{T}} & a\boldsymbol{u} + e\boldsymbol{Q}\boldsymbol{u}\\ \boldsymbol{u}_2^{\mathrm{T}} - \dfrac{1}{\rho+e}\boldsymbol{u}_2^{\mathrm{T}} & -a\boldsymbol{u} + e\boldsymbol{Q}\boldsymbol{u}\end{bmatrix}^{\mathrm{T}}, \quad \dot{\boldsymbol{q}} = \begin{pmatrix}\dot{q}_1\\ \dot{q}_2\end{pmatrix}$$

where $\boldsymbol{J}$ is the Jacobian matrix mapping the velocity of point P to the sliding rates of the two RPR limbs.

3.2 Workspace analysis

As shown in Fig.3, the reachable workspace W of point P is the intersection of two subspaces enclosed by two curves when the RPR limb reaches its minimum and maximum values, $q_{\min}$ and $q_{\max}$. In practice, it is desirable for the robot to have a rectangular workspace with a large width/height ratio. There exists in W a rectangle, $2d$ in width (y-axis) and h in height (z-axis), which is tangential to the inner bound of W at T_1 and T_2, and intersects with the outer bound of W at Q_1 and Q_2. This rectangular area is then defined as task workspace of the robot, denoted by W_t. Thus, given a, b, H, e, d and h, the extreme values of the RP and RPR limbs can be determined by considering the central and extreme alignments shown on Fig.3 as

$$\rho_{\min} = H\ ,\quad \rho_{\max} = \sqrt{q_{\max}^2 - (b-a)^2} \tag{6}$$

$$q_{\min} = \sqrt{b - a^{\,2} + H^2}\ , \quad q_{\max} = \sqrt{\begin{matrix}\rho_Q^2 + a^2 + b^2 + \\ 2b\ \ \rho_Q \sin\theta_Q - a\cos\theta_Q\end{matrix}} \tag{7}$$

where

$$\rho_Q = \sqrt{z_T + h^{\,2} + d^2} - e\,, \quad \theta_T = \tan^{-1}\left(\frac{d}{z_T + h}\right), \quad z_T = e + \rho_T\ \cos\theta_T\,.$$

ρ_T and θ_T satisfy the kinematic and boundary constraints

$$q_{\min}^2 - \rho_T^2 - a^2 - b^2 + 2b\ \ \rho_T \sin\theta_T + a\cos\theta_T\ \ = 0$$

$$b\cos\theta_T\ \ \rho_T\cos\theta_T - a\sin\theta_T\ \ - \ e + \rho_T\ \ \sin\theta_T\ \ \rho_T - b\sin\theta_T\ \ = 0$$

3.3 Optimal design

The optimal design formulation for the 2-DOF parallel mechanism can be stated as: given d and h, determine a, b, e and H such that good overall kinematic performance is achieved subject to a set of appropriate structural constraints.

It is well accepted that the most suitable local conditioning index for evaluating velocity, accuracy and rigidity performance is the condition number κ $(1 \le \kappa < \infty)$ of the Jacobian matrix [12]. Since κ varies with the system configuration, a weighted global conditioning index is proposed as an objective function for minimization, namely

$$\eta = \sqrt{\bar{\kappa}^2 + w\tilde{\kappa}^2} \tag{8}$$

where

$$\bar{\kappa} = \frac{\int_{W_t} \kappa \mathrm{ds}}{\int_{W_t} \mathrm{ds}}\,, \quad \tilde{\kappa} = \sqrt{\frac{\int_{W_t} \kappa - \bar{\kappa}^{\ 2}\,\mathrm{ds}}{\int_{W_t} \mathrm{ds}}}$$

$\bar{\kappa}$ and $\tilde{\kappa}$ represent, respectively, the mean and standard deviation of κ throughout W_t, w is a weighting to balance the relative significance between $\bar{\kappa}$ and $\tilde{\kappa}$.

The influence of the dimensional parameters on $\bar{\kappa}$ and $\tilde{\kappa}$ was investigated using non-dimensional groups referenced to b such that $\lambda_d = d/b$, $\lambda_a = a/b$, $\lambda_H = H/b$, $\lambda_h = h/d$, and $\lambda_e = e/a$. Two geometric constraints have been considered, i.e. (1) $\lambda_{q\min} \le \lambda_q = q_{\max}/q_{\min} \le \lambda_{q\max}$ allowing the RPR limb to have sufficient bending stiffness at one extreme and to have sufficient room to install the servomotor at the other; and (2) $\lambda_a \ge \lambda_{a\min}$ so that the platform has sufficient room to locate the 2-DOF rotating head without mechanical interference.

Taking $\lambda_d = 1.67$, $\lambda_h = 0.32$, $\lambda_e = 0.9$ and $w = 1$, Fig. 4 shows that η increases with increasing λ_H and λ_a. Having relatively small λ_a and λ_H is helpful for achieving a better kinematic performance, subject to the constraint $\lambda_q = \lambda_{q\max}$. For a practical design, accounting for workpiece and end-effector sizes, we take $d = 1.25\,\mathrm{m}$, $h = 0.4\,\mathrm{m}$ and $\lambda_q = \lambda_{q\max} = 1.9$ with λ_d and λ_e having the values given above. Table 1 shows the resulting dimensional parameters of the robot. Fig. 5 plots the condition number, κ, of the Jacobian: it has a minimum value of 2.64 at middle point of the inner bound and a maximum of 4.00 at the corner of the outer bound of the task workspace.

Table 1
Dimensional parameters of the Bicept (Units: mm)

a	b	H	e	$q_{\max}$	$q_{\min}$
330	750	1238	600	2483	1307

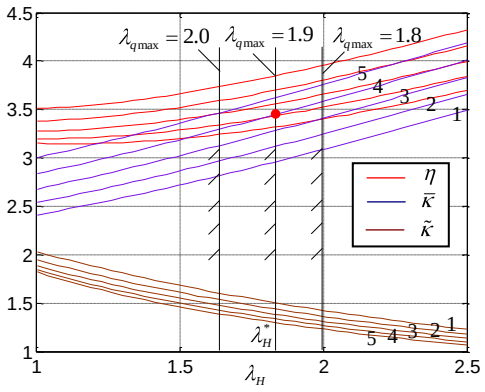

Fig.4 Variations of η, $\bar{\kappa}$ and $\tilde{\kappa}$ vs. λ_H and λ_a
$1: \lambda_a = 0.2,\ 2: \lambda_a = 0.4,\ 3: \lambda_a = 0.6,\ 4: \lambda_a = 0.8,\ 5: \lambda_a = 1.0$

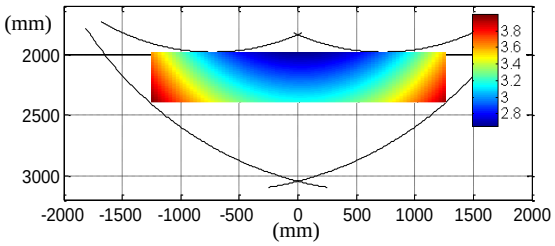

Fig.5 Condition number distribution in W_t

4. Performance evaluation

Based on the kinematic design, a detailed mechanical design leads to a virtual prototype shown in Fig. 1. Then, rigid body dynamics and stiffness analyses are carried out for motor sizing and stiffness prediction.

4.1 Motor sizing

The dynamic simulation software "CosmosMotion" embedded in SolidWorks, was used for rigid body dynamic analysis of the 2-DOF parallel mechanism in order to determine the maximum and rated speed, torque and power of its servomotors.

The simulation accounted for both gravitational and inertial loads of all movable components. The trajectory of point P was set as a straight-line starting from the top and ending at the bottom of the mid-line of the task workspace as shown in Fig.3, keeping the end-effector orientation always horizontal. Motion control used a piecewise rule such that P undergoes modified trapezoid motion in the acceleration/deceleration segments and has uniform motion in between. Specifying maximum acceleration/deceleration, $a_{\max} = 2\ \mathrm{m/s^2}$, and maximum uniform velocity, $v_{\max} = 0.5\mathrm{m/s}$, for point P, the angular velocity and torque of the two servomotors was determined by the ADAMS dynamic solver embedded within "CosmosMotion". Fig. 6 shows the driving torque to be composed of two components, 44% arising from the inertial load during acceleration and deceleration, and 56% arising from gravitational load if the robot is placed as shown in Fig.1; both vary with the system configuration. Thus, allowing up to 15% redundancy, the servomotor parameters in Table 2 can be specified to achieve up to $a_{\max} = 2\ \mathrm{m/s^2}$ and $v_{\max} = 0.5\mathrm{m/s}$ throughout the entire task workspace.

Table 2

Servomotor specifications*

Rated torque (Nm)	40
Peak torque (Nm)	160
Rated speed (rpm)	2000
Max. speed (rpm)	3000
Rated power (kW)	8
Moment of Inertia (10^{-3}kgm^2)	7.69

* with lead screw pitch of 12mm

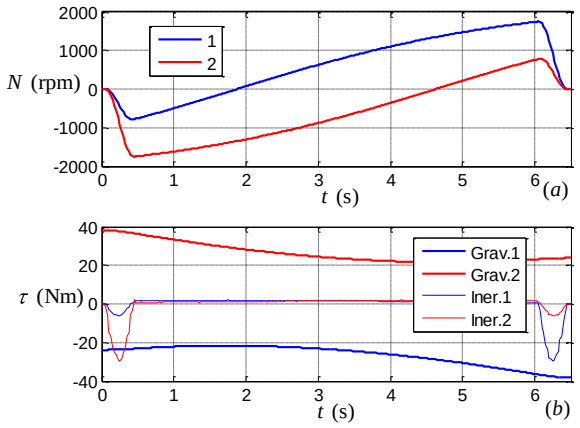

Fig.6 Rotational speed and driving torque vs. time of the servomotors as the robot travels from the top to the bottom of the workspace along a straight line
(a) Rotational speed (b) Driving torque

4.2 Stiffness evaluation

The 3D solid model generated by SolidWorks was exported to ANSYS to carry out a finite element stiffness analysis. Computational results at two typical configurations are listed in Table 3 and depicted in Fig. 7. It is observed that: (1) the stiffness varies with system configurations; (2) the stiffnesses at the center of the task workspace (configuration 1) are higher than those at the top middle point (configuration 2); and (3) the stiffness along the z axis is much higher than those along the other two orthogonal axes at all configurations, meaning that the robot is particularly suitable for drilling and riveting manipulations where high rigidity along the z axis is the primary consideration.

Table 3
Results of stiffness analysis

	Along x (N/μm)	Along y (N/μm)	Along z (N/μm)	About z ($\times 10^5$Nm/rad)
Configuration 1	2.67	5.02	108.87	7.49
Configuration 2	2.22	4.51	11.22	4.52

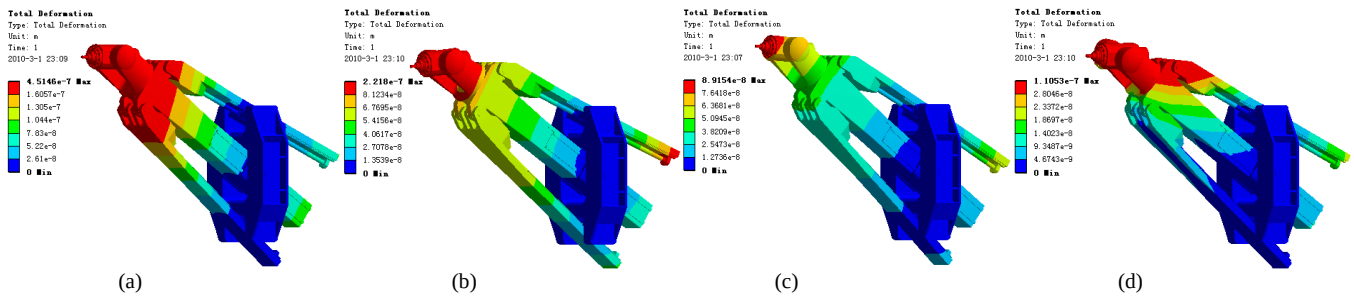

(a) (b) (c) (d)

Fig.7 Deformation of the point P under unit force or moment at the top of the middle layer of the task workspace
(a) along the x axis, (b) along the y axis, (c) along the z axis, and (d) about the z axis

5. Conclusions

The modular design of the Bicept enables configuration of a robot cell such that two cells placed face-to-face can form a wing box assembly system by adding translational motions along the long reference tracks. For a rectangular task workspace of $\lambda_d = 1.6 \sim 1.8$ and $\lambda_h = 0.25 \sim 0.3$, $\lambda_a = 0.4$ and $\lambda_q = 1.8 \sim 1.9$ are sensible design choices for providing a large workspace/machine volume ratio and relatively good kinematic performance. If the robot is to operate in a vertical plane, care should be taken to reduce its weight in order to reduce the static torque of the servomotors. The proposed design allows a very high rigidity along the z axis to be achieved for drilling and riveting operations.

6. Acknowledgements

This work is partially supported by NSFC (Grant No. 50535010, 50775158) and MOST (Grant No.2006BAF01B00).

7. References

[1] Rooks, R., 2001, Automatic Wing Box Assembly Developments, Ind. Robot, 28(4): 297-301.
[2] Webb, P., Eastwood, S., Jayaweera, N. and Chen, Y., 2005, Automated Aerostructure, Assembly, Ind. Robot, 32(5): 383-387.
[3] Murman, E. M., Walton, M., Rebentisch, E., 2000, Challenges in the Better, Faster, Cheaper Era of Aeronautical Engineering and Manufacturing, Aeronaut. J., 481–488.
[4] Perron, C., 2009, Aircraft Assembly, available at: http://www. nrc-cnrc. gc.ca/eng/ facilities/iar/amtc/aircraft-assembly.html.
[5] Weber, A., 2009, High-Flying Robotics, available at: http://www. aint. com/news- high-flying- robotics.html
[6] Neumann, K. E., 2002, Tricept Application, In Proceedings-3rd Chemnitz Parallel Kinematics Seminar, Zwickau, Germany, 547-551.
[7] Weck, M., Staimer, D., 2002, Parallel Kinematic Machine Tools-Current State and Future Potentials, CIRP Ann., 51(2): 671-683.
[8] Dahlstrom, P., 1999, Assembly Robot for Wing, WO/1999/047415
[9] Huang, T., Li, M., Zhang, D. W., Zhao, X. M., 2003, 4-DOF Hybrid Robot, CN Patent 1439492.
[10] Li, M. Huang, T., et al., 2005, Conceptual Design and Dimensional Synthesis of a Reconfigurable Hybrid Robot, ASME J. Manuf. Sci. and Eng., 127(6): 647-654.
[11] Altintas, Y., Brecher, B., Weck, M., Witt, S., 2005, Virtual Machine Tool, CIRP Ann., 54(2): 651-674.
[12] Gosselin, C. M., Angeles, J., 1991, A Global Performance Index for the Kinematic Optimization of Robotic Manipulators," ASME J. Mech. Des., 113(3): 220-226.